Ocean Surface Pressure Fields from Satellite-Sensed Winds

ROBERT A. BROWN AND GAD LEVY

Department of Atmospheric Sciences, University of Washington, Seattle, WA 98195

(Manuscript received 15 October 1985, in final form 4 May 1986)

ABSTRACT

The University of Washington's planetary boundary layer model is inverted to use remotely sensed satellite scatterometer-derived surface winds as input to calculate maritime surface pressure fields. The analysis of three different synoptic storm situations is performed using the model and is then compared to conventional National Weather Service analyses. Agreement is good. Isolation of the PBL secondary flow, stratification and thermal wind effects in the model revealed that each may be significant under certain conditions. However, the model shows sensitivity to the thermodynamic features only in a general sense and even a neutral stratification solution gives a good approximation. The high density of the scatterometer data produces mesoscale (hundreds of kilometers) dynamic details, which cannot be confirmed by conventional data at this stage.

1. Introduction

a. The satellite scatterometer data

It is evident that satellite-borne microwave sensors can contribute greatly to oceanographic and atmospheric research and operations. In particular, the scatterometer's capability to measure the surface wind or stress vector provides a basic dataset which has never existed before. It is often not clear exactly how to use this voluminous information. Classic models for the ocean and atmosphere have not been able to assume that the winds, stress and sea-surface temperature were known on scales of hundreds of kilometers to global except in gross climatological averages. The scatterometer signal responds to some measure of ocean surface roughness in the capillary and short gravity wave (and perhaps white water) regime. The mechanisms and energetics of the wind relation to this roughness have yet to be understood or even well defined.

However, this gap in our knowledge of the detailed physics of the radar signal-wind/stress correlation is somewhat moot in light of the verification of microwave signal to surface wind correlations established for the SEASAT-A scatterometer (SASS) as discussed by Jones et al. (1982) and Brown (1983). The next generation of satellite scatterometer will be flown on the NROSS satellite scheduled for a 1990 launch. This scatterometer (NSCAT) will have six antennas for wind direction discernment and a 25 km windfield discrimination. This data will reveal mesoscale phenomena in unprecedented detail. For instance, the midlatitude storm is an important regime which will be seen in this new perspective.

The microwave radar emits energy in wavelengths which are Bragg-scattered from ocean waves with a few centimeters wavelength. The strength of the return signal is related to the amplitude and density of the wind generated waves. Moreover, the backscatter is nonisotropic; and wind direction can be derived from radar measurements at different azimuths. SASS obtained two azimuthal looks on each side of the satellite by four dual polarized fan beam antennas that were aligned to point 45° and 135° relative to the satellite subtrack. A given surface location was first viewed by the forward antenna, and then approximately 1–3 minutes later it was viewed orthogonally by the aft beam. This resulted in up to four possible solutions for the wind directions and speeds. There is no a priori reason to prefer any of the solutions, and this is a major difficulty in the interpretation of SASS data.

The model function correlating the surface wind to the radar backscatter measurements has evolved and improved since the SEASAT mission. Some problems that had to be resolved include those concerned with different averaging of the SASS winds (over 17 × 70 km cells), colocation of the two looks (within 50 km), surface measurements accuracy (averaging times and sparse data limitations), the distortion of the Doppler cells due to geographical location, difference in polarization, attenuation in precipitation areas and lack of high wind data.

The final demonstrated accuracy of SASS winds on a mean synoptic scale as reported in the *Seasat Data Utilization Project Report* is ± 1.3 m s^{-1} and $\pm 16°$ for winds in the range of 4–26 m s^{-1}. Thus SASS produces mean winds on a synoptic scale commensurate with a dedicated oceanic experiment including weatherships and buoys as detailed by Nuss and Brown (personal communication, 1985). The main source of data for this research is the SASS dataset of surface winds derived from backscatter measurements over the ocean

during the 106 days (26 June 1978–10 October 1978) of its mission.

b. Applications

There are many oceanic mixed layer models and surface and internal wave generation mechanisms which are associated with the maritime storm regimes. It has been shown that the mixed layer, inertial current and gravity wave generation, the internal waves and the pycnocline can all change markedly with the passage of a storm. The horizontal variability on the 20–400 km scale plays an important part in the dynamics of the upper ocean. Simple one-dimensional ocean mixed layer models can be parameterized to work in particular regimes. However better stress parameterization or the use of two- or three-dimensional models are needed in this domain (Martin, 1986). There is evidence of strong atmospheric forcing on these scales in the storms regimes (Houze and Hobbs, 1982).

The analysis of the Storms Response Experiment (STREX) data has posed a number of interesting questions. The mesoscale variability in both atmosphere and ocean was found to be very large. The windfields were calculated by both the PBL model of Brown and Liu (1982) and in a kinematic analysis. These were compared by Nuss and Brown (personal communication, 1985). The conclusions of these and other papers (Bond and Fleagle, 1985) are that important atmospheric dynamics take place on scales that are not practically resolvable with conventional methods. The windfields provided the mesoscale variation in the stress fields for the oceanic internal wave and inertial current generation models of D'Asaro (1985) and the basic driving force for mixed layer models such as Niiler's (1975). In STREX a new inertial current regime of 25 cm s^{-1} was set up in the mixed layer by a storm. While mixed layer models exist to predict these currents, thermocline deepening and energetics of the layer, they await more detailed stress measurements to evaluate them. Better determination of the winds, stress, sea surface temperature and frontal location are essential for progress in these mesoscale modeling efforts. Nuss and Brown concluded that the primary limitation on the accuracy of the models was the sparsity of the input data. With the development of satellite scatterometer data such as NSCAT, windfields on a 25 to 50 km grid will be available. This will allow extraordinary detail in the mesoscale fields. In order to relate this data to conventional analyses a good representation of the relation between the surface stress, roughness, stratification, PBL winds and the upper level flow with corresponding pressure fields must be established.

Endlich et al. (1981) used the SASS data together with GOES-2 cloud motion data and the balance equation to calculate pressure fields with good success. When the SASS surface winds are used as a lower boundary condition to a model for the flow variation through the boundary layer, the geostrophic wind can be calculated with good accuracy. The pressure gradient field can then be used with a single pressure measurement to calculate a surface pressure field.

The independently deduced surface pressure fields for STREX were in substantial agreement (0.5 mb) for fairly uniform synoptic fields but exhibited differences of several millibars in the vicinity of a front. The frontal location and mesoscale dynamics of midlatitude storm systems are difficult to define with conventional analysis. Since the storms regime and fronts are an important weather phenomena and produce significant air–sea interaction and PBL fluxes, we have concentrated our analyses on these cases.

2. The planetary boundary layer model

a. Basic model results

In order to use the scatterometer surface wind data to obtain the wind profile throughout the PBL, a model including basic dynamics is needed. While there are many models for specific scales and conditions of the PBL, few are compatible with the specific scatterometer data. The University of Washington two-layer similarity model was designed to produce vertical velocity profiles and surface stress from gradient winds on a 50–100 km grid. This model has been successfully used in several major experiments. It includes: a surface layer with Businger/Dyer stratification corrections (Paulson; 1970); a matched Ekman layer modified with explicitly modeled large eddies which vary with layer stratification as discussed by Brown (1970, 1972) and LeMone (1973); a variable ocean surface roughness parameterization; humidity effect; and a thermal wind correction. The unique capability of the model in accounting for the large eddies in the Ekman layer and thereby the effects of stratification in this layer is important whenever near surface winds or stress are used to relate to higher level winds. Thus, the relation between surface stress or surface layer winds to geostrophic winds depends on the stratification and dynamics of the entire boundary layer as discussed by Brown and Liu (1982). This model was tested in the SEASAT-A workshop against two other mesoscale models: a two-layer version lacking only the Ekman layer secondary flows, and a constant wind ratio, constant turning angle "model." When stratification varied in the region, such as in the North Pacific area studied by the Gulf of Alaska Seasat Experiment (GOASEX), this model had better agreement than the others in comparisons with surface observations (NASA, 1980). The model was used in the GOASEX and the Joint Air–Sea Interaction Experiment (JASIN) to calculate comparison winds for the SEASAT-A scatterometer (SASS) (Brown et al., 1982).

The PBL secondary flows are a prominent and omnipresent feature of storm environments—the cyclones, hurricanes and polar lows are notable examples. How-

ever they are also present whenever winds are greater than 5–10 m s^{-1} (depending on stratification), as recorded in Brown (1980), Walter (1980) and Walter and Overland (1984). The flux mechanisms of the boundary layers (air and sea) can be quite different for regimes with or without secondary flow. The large effect of organized flows on fluxes is discussed by Overland and Wilson (1984).

When this model is inverted, scatterometer winds or stress serve as an input to obtain the geostrophic winds and thus to calculate surface pressure fields. Since the relation between surface winds and geostrophic winds is quite variable with stratification, the PBL model is essential to obtaining accurate pressures. Figure 1 shows the variation in $U_{19.5}/G$ and α with stratification calculated from the model. In a typical marine storm system, stratification will vary from unstable to stable in various sectors. It is clear that variation in these parameters will yield significantly different results from a model employing constants for these parameters.

b. *The model characteristics*

The SASS winds are cataloged at 19.5 meters height for neutral stratification. Corrections for variable mast heights in the dataset for parameterization were made with the neutral atmospheric log layer formulation,

$$V = (u^*/k)\ \ln(1950/Z_0) \qquad (1)$$

where

V SASS data record wind
k Von Karman's constant = 0.4
u^* the surface layer friction velocity
Z_0 a roughness parameter, depending on u^* empirically determined.

This relation is inverted to determine u^*. It requires an iteration on $Z_0(u^*)$.

The velocity in the PBL is given by the modified Ekman–Taylor solution,

$$U = \cos\alpha + u_t Z + e^{-Z}[(\cos Z - \sin Z)\sin\alpha + v_t \cos Z] + U_2$$

$$V = \sin\alpha + v_t Z - e^{-Z}[(\cos Z + \sin Z)\sin\alpha + v_t \sin Z] + V_2$$

where

$$(U_g, V_g) = (\cos\alpha, \sin\alpha) + (u_t, v_t)Z.$$

The vector wind $\mathbf{U}_2 = (U_2, V_2)$ is the modification to the Ekman/Taylor mean flow solution to account for stratification dependent secondary flow as determined by Brown (1970, 1972). The thermal wind, $\mathbf{V}_t = (u_t, v_t)$, is related to the horizontal air temperature gradient. The subscripts x, y and z denote partial differentiation; g denotes geostrophic, t is thermal wind, 2 is secondary flow and 0 denotes near surface values. The velocities are nondimensionalized with $U = U/u^*$, and $Z = z/\delta$, where δ is $(2Kf)^{1/2}$, K is a mean eddy-viscosity for the PBL, f is the Coriolis parameter.

The two layers are matched to yield a single parameter similarity relation which enables the entire velocity profile to be determined. The neutrally stratified profile can be corrected for stratification, thermal wind and humidity effects with the additional input of air and sea temperatures and relative humidity.

The "inverse" model was tested against the "direct"

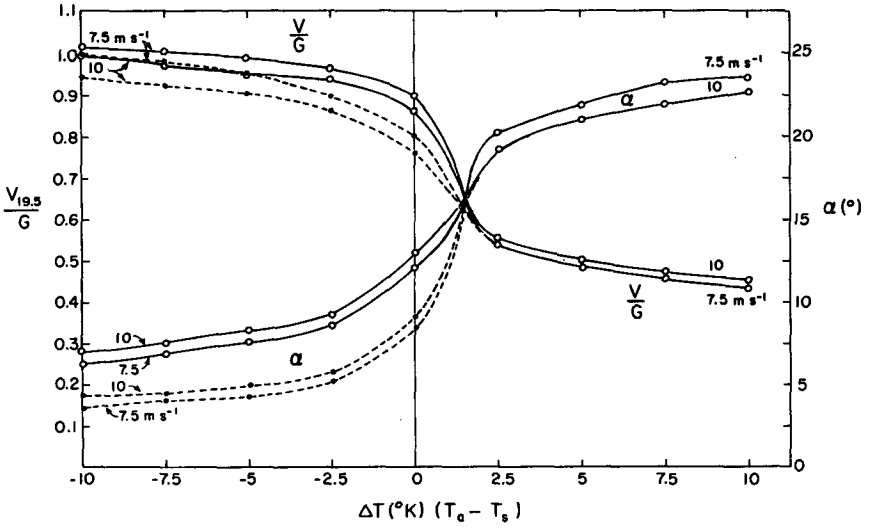

FIG. 1. Model results for the variation of the turning angle (α) and the wind at 19.5 m (V/G) with stratification ($\Delta T = T_a - T_s$ where T_a and T_s are air and sea temperatures, respectively) for two different wind speeds (7.5 m s^{-1}; 10 m s^{-1}), with (solid) and without (dashed) secondary flows.

model from Brown and Liu and reproduced the basic results shown in Fig. 1. The main features include the sharp gradients in the ratio of surface winds to geostrophic level winds and in turning angle near the neutral stratification region. The effect of humidity is to move the sharpest gradients toward stable stratification due to the increased buoyancy of the moist parcels. The dashed lines are obtained when secondary flow is omitted.

In the inverse model (pressure fields from surface winds) the input winds and thermodynamic data must be appropriately gridded. In the case of conventional data this requires elaborate interpolation and extrapolation to account for generally sparse datasets. While this is still true for the thermodynamic variables in our study, the SASS wind data present different problems.

SASS took measurements on each side of its subtrack with a line of nadir winds (with no directions) along the subtrack. Winds were determined in a swath from approximately 200–700 km to each side. Optimum resolution in this region was about 50 km. Subsequent adjacent revolutions produced strips separated by 0–1000 km and 100 minutes depending on latitude. At the midlatitudes of our study, this yielded a gap of 0–400 km between subsequent orbits. The areas in between swaths were filled in by interpolation, whereby a gridpoint value was assigned based on a weighted average of all measurements within a variable radius of influence. The method is described in Levy and Brown (1986).

Although the problem of ambiguity removal in the four wind directions will be mostly resolved in NSCAT, it exists in SASS data used here. We have removed the ambiguities using a method similar to Hoffman (1982, 1984) and reported in Levy and Brown (1986). In order not to compromise the resulting pressures by correcting successively on a first-guess pressure field, a SASS alias closest to a first-guess wind was chosen and not changed subsequently. Some sort of independent information is needed for the dealiasing of the SASS data.

The similarity functions from Brown and Liu (1982) are

$$B = (1 - \lambda\psi)/(2\lambda) \tag{3}$$

$$A = \psi - B - \ln[\delta\lambda/Z_0] \tag{4}$$

$$\beta = (v_t - u_t + V_2 - U_2)/2 \tag{5}$$

$$\gamma = (V_t + U_t + V_2 + U_2)/2. \tag{6}$$

The matching relations yield,

$$\delta = 2k\lambda U_*/f[1 - \lambda\psi(Z/L)] \tag{7}$$

$$(U_t, V_t) = g\delta(-T_y, T_x)/(f T_0 G). \tag{8}$$

The single similarity parameter $\lambda = 0.15$, and ψ is the log layer stratification parameter from Businger/Dyer depending on the ratio Z/L where L is the Obukhov length,

$$L = T_0 u^{*2}/(gkT^*) \tag{9}$$

and T^* = scaling temperature (virtual) for the surface layer.

The angle of turning can be solved from

$$B/A = (\sin\alpha + \beta)/(\cos\alpha + \gamma). \tag{10}$$

The geostrophic wind magnitude and corresponding pressure field is obtained from

$$G = -Bu^*/[k(\sin\alpha + \beta)] = -Au^*/[k(\cos\alpha + \gamma)] \tag{11}$$

where β and γ are dependent on thermal wind and secondary flow, and

$$\left[\frac{\partial P}{\partial x}\right] = (\rho f V_g); \quad \left[\frac{\partial P}{\partial y}\right] = -(\rho f U_g) \tag{12}$$

$$P = \int (\partial P/\partial x)dx + \int (\partial P/\partial y)dy + P_0. \tag{13}$$

An independent value of P_0 is needed to establish the magnitudes. It is convenient to define a neutral drag coefficient, $C_{d_{10}} = (u^*/U_{10})^2$. From (1), this is dependent on Z_0 only. Figure 2 shows the model relation for the neutral drag coefficient (and hence the roughness variation) versus wind and stratification taken from Brown and Liu.

There is an increase in roughness for increased wind or unstable stratification due to increased momentum transfer to the surface. The radar backscatter is proportional to the capillary and short gravity wave density, height and shape. This reflects the momentum transfer from the air to the sea surface and is directly represented in the surface stress, $\tau = \rho u^{*2}$. The velocity profile will vary with roughness and stratification. For a given scatterometer reading, u^{*2} is constant. The dashed lines in Fig. 2 show the range of possible u and C_d for the same u^* (SASS signal) due to stratification effects. For example, if boundary layer stratification changes from $T_a - T_s = -5°$ to $+5°$, U_{10} is 5.7 to 7.5

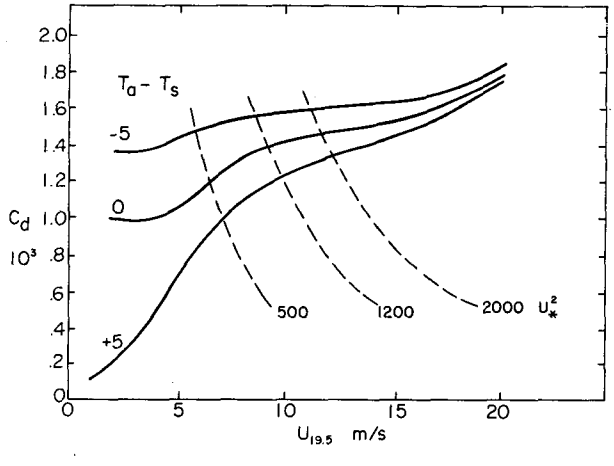

FIG. 2. The model parameterization of drag coefficient (C_d) versus the 19.5 m height winds ($U_{19.5}$) for three different stratifications ($T_a - T_s$). Lines of constant stress (U_*^2) are also marked by dashed lines.

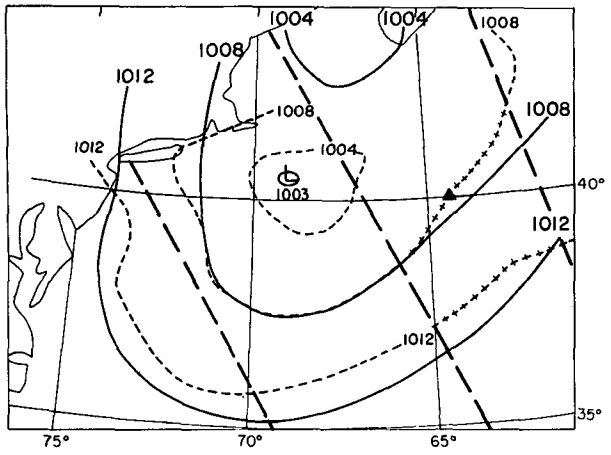

FIG. 3. Conventional pressure analysis (solid) based on Gyakum's (1983a) reanalysis compared to basic neutral model derived fields based on SASS measurements (dashed) for 1200 GMT 9 September 1978. The bold dashed lines mark the Seasat subtrack boundaries (between 63° and 69°W and again in the northeastern corner). The crossed lines mark contours in areas where no SASS data were available and interpolation was done. The triangle denotes the location of the pressure measurement used as P_0.

m s^{-1} for $u^{*2} = 500$ (cm s^{-1})^2 (6 to 8 m s^{-1} at 20 meters height) or 11.1 to 12.5 m s^{-1} (12 to 13.4 m s^{-1} at 20 m) for $u^{*2} = 2000$ (cm s^{-1})^2. (The range of $1.52 < C_d \times 10^3 < 0.91$ is much greater). Thus the variation in surface layer winds due to stratification effects is 1–2 m s^{-1}.

On the other hand, from Fig. 1, the variation in the ratio $U_{19.5}/G$ and α over the same range of stratification is considerable. Thus for the same surface radar backscatter, $12.6 < G < 26.8$ m s^{-1} and $7° < \alpha < 22°$ for $-5° < T_a - T_s < +5°$. It is difficult to translate these variations into the integrated effect on a pressure field. In regions of strong gradients of surface winds and temperatures the contribution is expected to be significant. We have run each case with and without surface layer and Ekman layer stratification, humidity and thermal wind effects to indicate their respective importance.

3. Results

The storm of 9–10 September 1978 in the west Atlantic provided an example of rapid cyclogenesis such that it did not appear in the National Weather Service (NWS) prognosis. Subsequent analysis has been done by Gyakum (1983a,b) and the SASS neutral model derived pressure fields are compared with this analysis in Fig. 3. There is a time difference of 55 minutes between Gyakum's analysis (solid) and the SASS swath used for the model analysis (dashed). However, at the time the surface low was still quite shallow and the changes during that time are not expected to be large. The SASS derived pressure solution presented in Fig. 3 represents a basic neutral solution that could be improved by inclusion of thermodynamic corrections. A notable distortion of the 1008 mb isobar occurs along the coastline of Long Island due to the proximity of land. SASS measurements were averaged into cells approximately 17 × 70 km and thus data within 70 km from the coastline should be discarded. The short-wave perturbation in the eastern sector near the SASS swath edge is apparently due to discontinuities in the dealiasing of wind directions.

On 14 September 1978, the Seasat passed twice over a storm in the northeast Pacific. The separation in time between the swaths was approximately 90 minutes (orbit 1040 at 1718 GMT and orbit 1041 at 1850 GMT) and we base our analysis on these two orbits. The infrared satellite image of the Gulf of Alaska at 1745 GMT 14 September 78 is shown in Fig. 4. The corresponding NWS surface pressure analysis at 1800

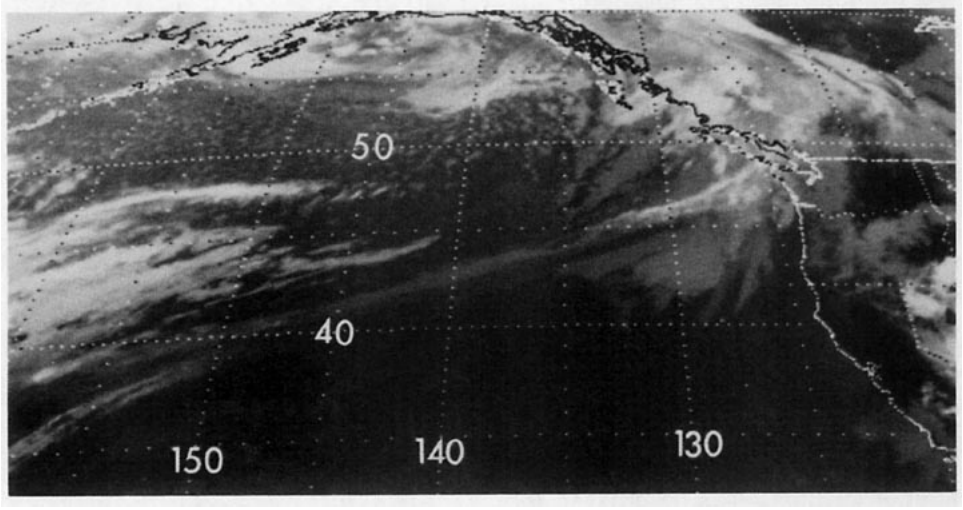

FIG. 4. Infrared satellite image for the Gulf of Alaska at 1745 GMT 14 September 1978.

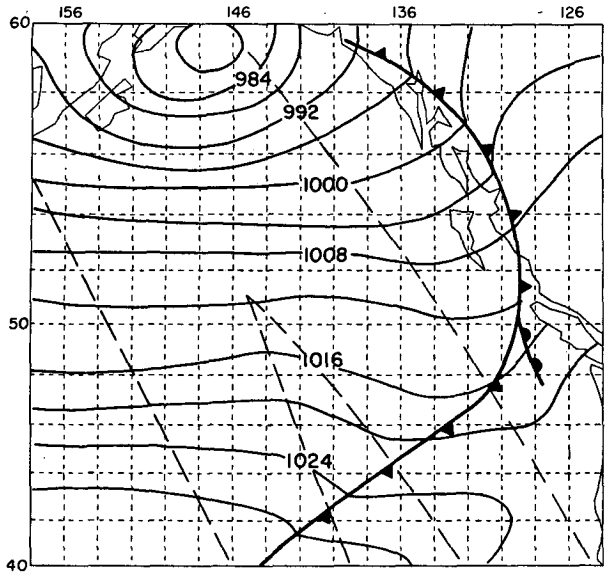

FIG. 5. NWS surface pressure analysis for 1800 GMT 14 September 1978. Dashed diagonal lines mark the SASS wind measurement areas comprised of two intersecting swaths from separate orbits.

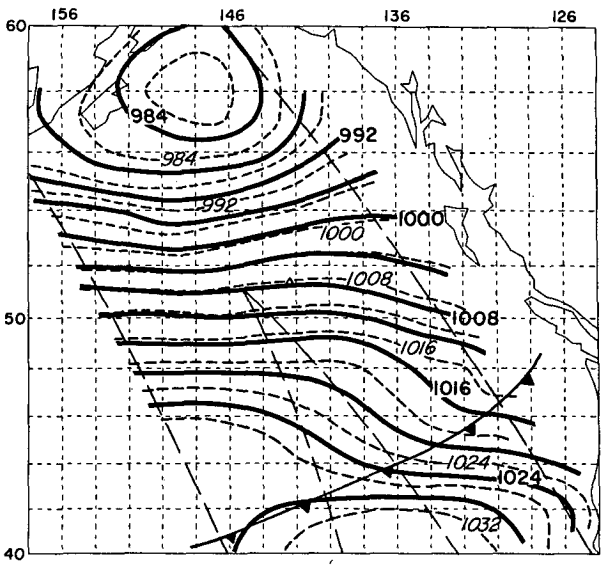

FIG. 6. Model derived pressures based on SASS measurements and one pressure measurement (triangle at 52°N, 142.5°W) with cold front relocated per satellite data. Solid lines are isobars for neutral analysis with secondary flow, dashed contours denote analysis without secondary flow in the Ekman layer.

GMT is shown in Fig. 5. The field is fairly uniform between the low and the front. The area enclosed by the outer dashed lines is dense in SASS wind measurements. The wedge to the south appears as the two orbital swaths diverge.

Figure 6 shows the SASS derived pressure fields under the neutral stratification condition (solid) compared to the case without secondary flow modification (dashed). In the SASS derived fields the low pressure center is located approximately 1.5 deg south and one deg west of the low pressure center in Fig. 5. The satellite image supports this position. Based on the satellite image and in agreement with SASS data, we have changed the location and orientation of the cold front translating it 0–2 deg longitude. The maximum amplitude of the troughing between 44° and 50°N is increased from 2 to 3 deg latitude when SASS data are used. The addition of secondary circulation in the neutral solution caused an increase of two mb in the minimum central pressure and pushed the isobars northward in the northern part of the domain and southward in the southern part of the domain reducing the overall north–south pressure gradient across the domain to closer agreement with the NWS map. The highest pressure contour was reduced by four millibars (in agreement with NWS analysis).

Air–sea temperature differences range from +1° in the low center and ahead of the front, to −1° in the center of the region shown. The effects of this moderate stratification are shown in Fig. 7. Minor changes occurred in the central unstable region behind the front and some translation of the isobars occurred in the stable areas near the low center and ahead of the front. The addition of thermal wind effects did not affect the final pressure field in this case. We based our thermodynamic corrections on all available ship reports in the area (GOASEX experiment area).

The same area of the east Pacific was viewed again by the Seasat at 1730 GMT 17 September (rev 1083) and at 1910 GMT (rev 1084). This time the Seasat viewed a typical blocking situation with a high pressure

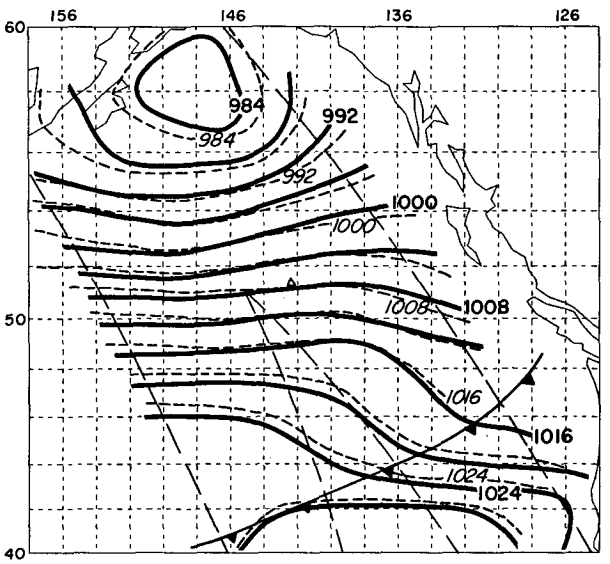

FIG. 7. The effect of stratification. As in Fig. 6 except that solid lines include stratification corrections and dashed lines do not.

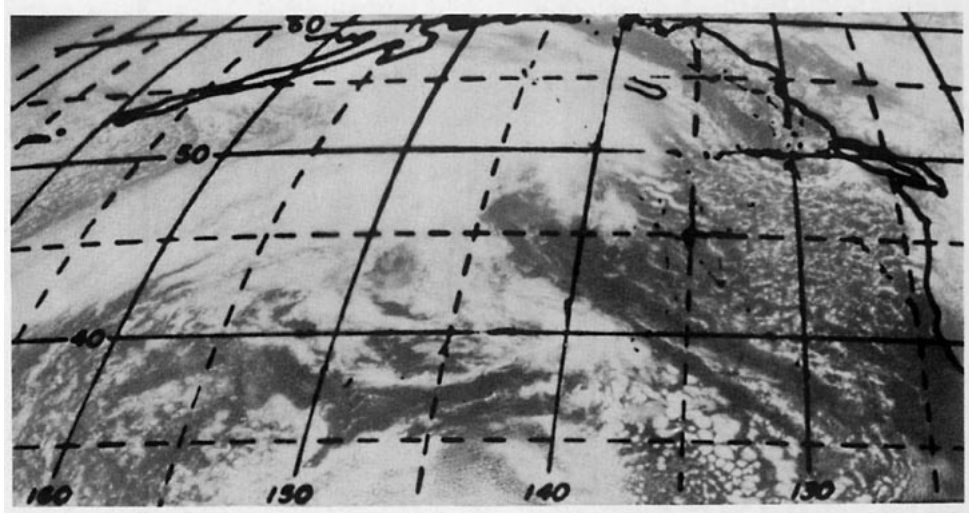

FIG. 8. Satellite visible image of the Gulf of Alaska at 1815 GMT 17 September 1978.

center to the east and the eastern edge of a stationary front (part of a "double low" system). The visible satellite image at 1815 GMT is shown in Fig. 8. Figure 9 shows the NWS analysis for that time with the boundaries of the SASS data marked by dashed lines. The region is dense in SASS winds from the low winds in the ridge to the high winds associated with the fronts. The geographic gap in data is smaller in this case. However, due to missing data in one of the orbits there is no region of overlap. Figure 10 displays the neutral stratification solutions and the effects of the secondary flow (solid). It is in good agreement with the NWS analysis (Fig. 9). In this case the secondary flow effects are minor and limited to areas of stronger winds. The short-wave variations in the model pressure fields seem to be a result of the SASS directional dealiasing procedure and curve fitting procedures in the model. The air–sea surface temperature difference based on ship and buoy reports is contoured in Fig. 11 and reflects the expected temperature advection pattern. There are stably stratified regions east of the ridge and in the warm sector of the frontal system. There is a meridional band of neutral to slightly unstable stratification in the center of the area. The unstable stratification appears to be east of the highest pressure where presumably the strongest advection is expected. These stratification gradients produce some changes in the pressure map as shown in Fig. 12. Constant pressure lines to the east of the high are moved eastward and those to the north are moved southward. In the sensitive divergent region

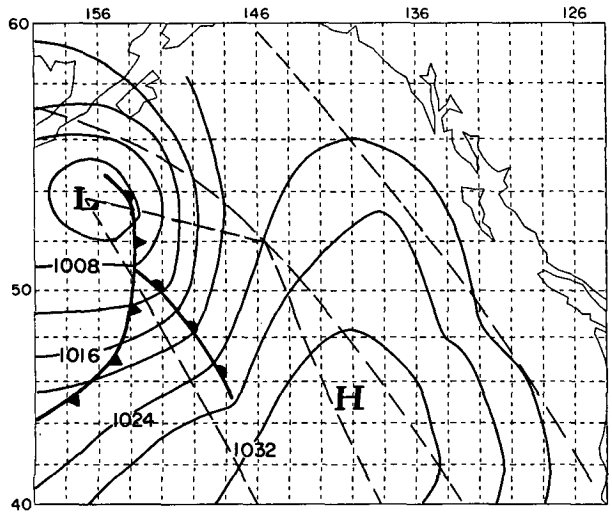

FIG. 9. As in Fig. 5 except for 17 September 1978.

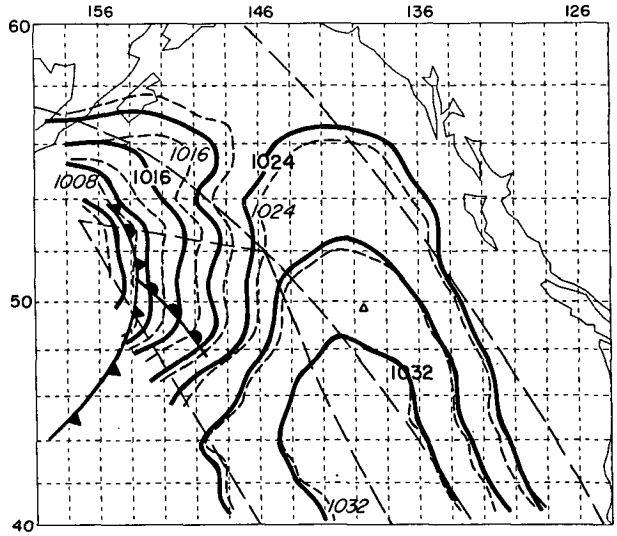

FIG. 10. The effect of secondary flow. As in Fig. 6 except for 17 September 1978.

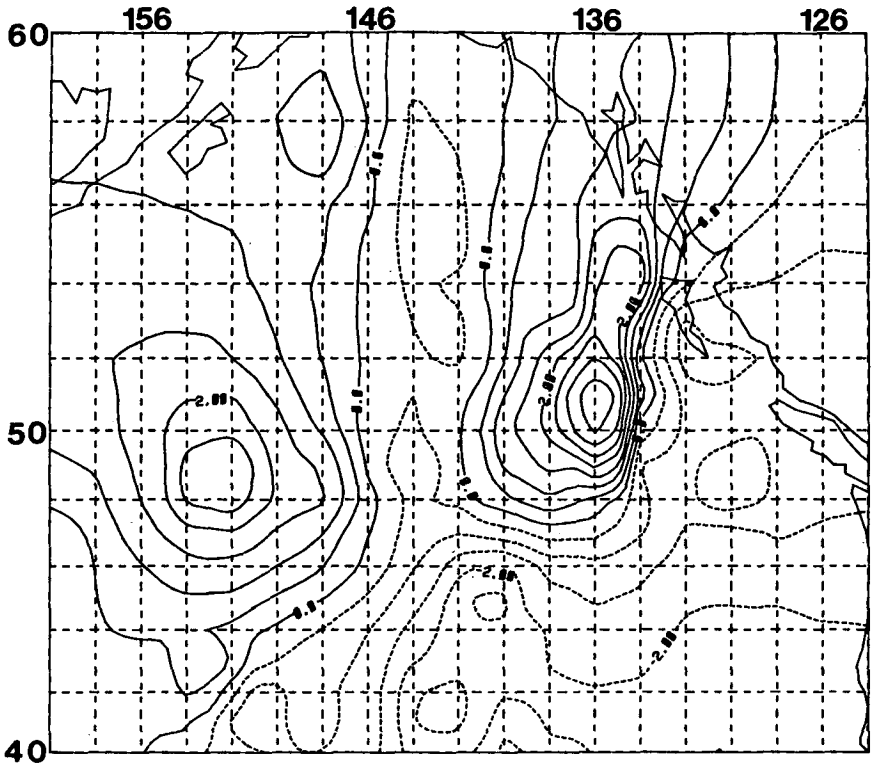

FIG. 11. Air–sea surface temperature difference contoured at 0.5°C on 1800 GMT 17 September 1978 based on ship and buoy reports. Solid lines are positive differences, dashed lines are negative values.

of the pressure field, the 1020 mb line now becomes part of the ridge. The low has been deepened further from the neutral analysis by about 4 mb. There are no reports at the center of the low that can independently support either analysis.

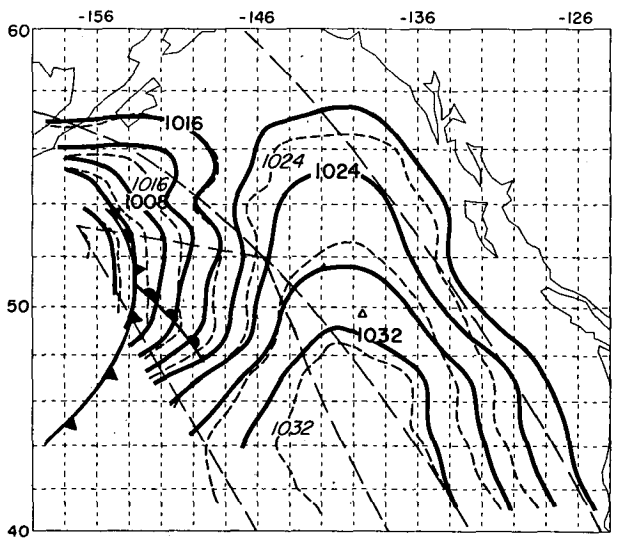

FIG. 12. The effect of stratification. As in Fig. 7 except for 17 September 1978.

We tested the sensitivity of the pressure fields to small changes in the thermodynamic field by applying different degrees of smoothing to the thermodynamic data, omitting and adding bad data points. As long as the overall structure stayed the same, the pressure field did not show any sensitivity to such alterations. In connection with the increased horizontal air temperature gradients, there is a thermal wind component which can affect the $U_{19.5}/G$ by 0–20%. Figure 13 compares the SASS derived fields with all effects included (solid) to the NWS analysis. The addition of the thermal wind effects restored the 1020 mb contour to a position slightly to the north of its original position and left the deeper low center (1000 mb isobar) unchanged.

4. Discussion

The comparisons between model analyzed pressure fields with various effects included gave some measure of the importance of each. We looked at three very dynamic fields of storms with fronts and variable stratification. One unique feature of our model, the variation of the Ekman layer due to secondary flows, showed changes of about 2–3 mb compared to the neutrally stratified layer without secondary flow. This magnitude of difference was also characteristic of the stratification effects, wherein the Ekman layer varied with stratification.

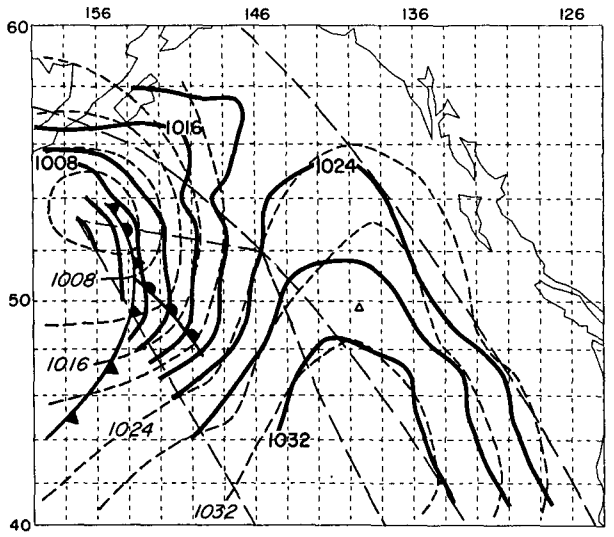

FIG. 13. Basic comparison. As in Fig. 12 except that the solid lines are model results with all corrections (secondary flow, stratification and thermal wind) and the dashed lines are the NWS analysis.

Stratification was not available in the 12 September Atlantic storm, but it was fairly uniform in the Pacific storm on 14 September and fairly significant on 17 September. This effect alone can amount to 4–5 mb variation in the fields. In contrast, the thermal wind effect was nil on the 14th and 1–2 mb on the 17th. This is partly because in high wind regions, the boundary layer is relatively thin, with little room for baroclinic forced variation.

When the results were compared to the NWS maps, there was basic qualitative agreement even for the model with minimum physics. However, in the limited cases studied, the addition of secondary flow, thermal wind and stratification each tended to improve the agreement with NWS analyses. In some cases, the less than 2 mb changes are not greater than the inherent accuracy of the best-fit fields, which can have errors of ±2 mb due to instrument accuracy limitations. The combined effects in the complete model sometimes canceled and sometimes added. This produced regions where the model differed by 4–5 mb from the NWS analysis. Since enough surface measurements are not available to independently check, the relative accuracies cannot be determined.

Short waves appear in the model isobars under different circumstances. Sensitivity tests indicate that these are sometimes due to the gridding and contouring procedures wherein polynomials are fit to the data. However careful attention to this procedure minimized this effect in the cases given. They may also be due to the nature of the dealiasing scheme which allows lines of relatively abrupt direction change where one branch of the four possible wind vectors is switched to another. The algorithm also experiences this abrupt transition in number of aliases from two to three or four. These changes can be smoothed out; however, in some areas the regular variation of the SASS wind vectors can produce similar wavelength variations. These might reflect a new regime of actual flow dynamics. Radar observations by Houze and Hobbs (1982) also indicate mesoscale variability of this scale in the fronts.

Improvements in the scatterometer algorithm will correct the effects of the abrupt transition in the solution, making it easier to discern the physical waves. The model can be modified to include gradient wind corrections in regions of large isobar curvature. Also, the divergence of the geostrophic windfield can be calculated to provide some measure of the accuracy of this nondivergent field. Only the examination of more detailed pressure fields can reveal which phenomena are model generated and which are real physical characteristics of these mesoscale wind and pressure fields.

The choice of one central pressure point as an integration constant was sufficient to carry out the integration to areas as large as 2000 km × 2000 km with a few mb error in very dynamic regions. This combined with the sensitivity of the pressures to only the gross thermodynamic fields gives merit to the idea that in areas where such data are unavailable, an assumed central pressure and thermodynamic field (based on scatterometer measurements and forecast fields) would result in qualitatively good analyses. It is evident from these initial results that this process applied to global scatterometer data can produce marine surface pressure maps of quality similar to that of the global ship and buoy collection procedure. While there are many limitations to the current scatterometer wind data, it appears that the accuracy is commensurate with the pressure field accuracy of the NWS analyses. This comparison was done in relatively high density ship report regions, and one might expect a significant improvement in sparse report areas such as the Southern Hemisphere. Further research is needed to explore this idea as well as additional sensitivity tests to establish the response of the model to different initial pressure inputs.

Acknowledgments. Support during this research was provided by NASA Grant NAGW-679.

REFERENCES

Bond, N. A., and R. G. Fleagle, 1985: Structure of a cold front over the ocean. *Quart. J. Roy. Meteor. Soc.*, **111**, 739–759.

Born, G. H., D. N. Held, D. B. Lame, R. G. Lipes, D. R. Montgomery, P. J. Rygh and J. F. Scott, 1982: *Seasat Data Utilization Project Rep.*, JPL D-36, NASA, Jet Propulsion Laboratory, Pasadena, 72 pp.

Brown, R. A., 1970: A secondary flow model for the planetary boundary layer. *J. Atmos. Sci.*, **27**, 742–757.

——, 1972: The inflection point instability problem for stratified rotating boundary layers. *J. Atmos. Sci.*, **29**, 850–859.

——, 1980: Longitudinal instabilities and secondary flows in the PBL: a review. *Rev. Geophys. Space Phys.*, **18**, 683–697.

——, 1983: On a satellite scatterometer as an anemometer. *J. Geophys. Res.*, **88**, 1663–1673.

——, 1986: On scatterometer capabilities in air–sea interaction. *J. Geophys. Res.*, **91,** 2221–2232.

——, and W. T. Liu, 1982: An operational large-scale marine PBL model. *J. Appl. Meteor.*, **21,** 261–269.

——, V. J. Cardone, T. Guymer, J. Hawkins, J. E. Overland, W. J. Pierson, S. Peteherych, J. C. Wilkerson, P. M. Woiceshyn and M. Wurtele, 1982: Surface wind analysis for SEASAT. *J. Geophys. Res.*, **87,** 3355–3364.

D'Asaro, E. A., 1985: The energy flux from the wind to near inertial motion in the surface mixed layer. *J. Phys. Oceanogr.*, **15,** 1043–1059.

Endlich, R. M., D. E. Wolf, C. T. Carlson and J. W. Maresca, Jr., 1981: Oceanic wind and balanced pressure-height fields derived from satellite measurements. *Mon. Wea. Rev.*, **109,** 2009–2016.

Gyakum, J. R., 1983a: On the evolution of the *QEII* storm. I: Synoptic aspects. *Mon. Wea. Rev.*, **111,** 1137–1155.

——, 1983b: On the evolution of the *QEII* storm. II: Dynamic and thermodynamic structure. *Mon. Wea. Rev.*, **111,** 1156–1173.

Hoffman, R. N., 1982: SASS wind ambiguity removal by direct minimization. *Mon. Wea. Rev.*, **110,** 434–445.

——, 1984: SASS wind ambiguity removal by direct minimization, Part II. *Mon. Wea. Rev.*, **112,** 1829–1852.

Houze, R. A., and P. V. Hobbs, 1982: Organization and structure of precipitating cloud systems. *Advances in Geophysics,* Vol. 24, Academic Press, 225–315.

Jones, W. L., L. C. Schroeder, D. H. Boggs, E. M. Bracalente, R. A. Brown, G. J. Dome, W. J. Pierson and F. J. Wentz, 1982: The geophysical evaluation of remotely sensed wind vectors over the ocean. *J. Geophys. Res.*, **87,** 3297–3317.

LeMone, M., 1973: The structure and dynamics of horizontal roll vortices in the PBL. *J. Atmos. Sci.*, **30,** 1077–1091.

Levy, G., and R. A. Brown, 1986: A simple objective analysis scheme for scatterometer data. *J. Geophys. Res.*, **91,** 5153–5158.

Martin, J. P., 1986: Simulation of the mixed layer at OWS November and Papa with several models. Submitted to *J. Phys. Oceanogr.*

NASA, 1980: Seasat Workshop Report, NASA, JPL Publ. 80-62. [Available from NASA, Jet Propulsion Laboratory, Pasadena, CA.]

Niiler, P., 1975: Deepening of the wind-mixed layer. *J. Marine Res.*, **33,** 405–422.

Overland, J. E., and J. G. Wilson, 1984: Mesoscale variability in marine winds at mid-latitude. *J. Geophys. Res.*, **89,** 10 599–10 614.

Paulson, C. A., 1970: The mathematical representation of wind speed and temperature profiles in the unstable atmospheric surface layer. *J. Appl. Meteor.*, **9,** 857–886.

Walter, B. A., 1980: Wintertime observations of roll clouds over the Bering Sea. *Mon. Wea. Rev.*, **108,** 2024–2031.

——, and J. E. Overland, 1984: Observations of longitudinal rolls in near neutral atmosphere. *Mon. Wea. Rev.*, **112,** 200–208.